Toward understanding slip inversion uncertainty and artifacts: 2. Singular value analysis

František Gallovič[1] and Jiří Zahradník[1]

Received 28 June 2010; revised 5 November 2010; accepted 10 December 2010; published 18 February 2011.

[1] Seismic slip inversion is studied by means of singular value decomposition (SVD), with emphasis on the role of singular vectors and regularization of the solution. Because the stable part of the slip inversion result is given in terms of a linear combination of the leading singular vectors (representing directions in the model space most sensitive to data), the performance of the inversion depends simply on how well the real slip model can be expanded into these vectors. The analysis is demonstrated using a synthetic model of a symmetric bilateral rupture with two asperities. Inverting the data yields a persisting false asperity in the middle of the fault, regardless of the inversion scheme used, because such a model cannot be well represented by only the leading singular vectors. The parallel study of the singular vectors from the individual stations and the whole network is suggested in order to understand how to achieve balance between overregularized solutions (with possible slip inversion artifacts) and underregularized solutions (vulnerable to data errors). The ideas are applied to the Mw 6.3 Movri Mountain earthquake, 2008, Greece, showing a weak indication of an asymmetric bilateral rupture. We suggest that inversion methods, not working explicitly with singular vectors, may yield artifacts, the origin of which can be also often explained by the SVD technique. Therefore, practical earthquake studies should be broadly complemented by the analysis of the leading singular vectors, a simple tool to evaluate the efficiency and potential drawbacks of the slip inversion.

Citation: Gallovič, F., and J. Zahradník (2011), Toward understanding slip inversion uncertainty and artifacts: 2. Singular value analysis, *J. Geophys. Res.*, *116*, B02309, doi:10.1029/2010JB007814.

1. Introduction

[2] Seismic slip inversion treated as a linear inverse problem is, in the literature, understood to be extremely unstable. Thus, the problem is typically stabilized by supplementing with nonlinear constraints, such as the positivity of the slip (or the slip velocity) and/or spatial-temporal smoothing [*Das et al.*, 1996; *Olson and Apsel*, 1982; *Hartzell and Heaton*, 1983; *Sekiguchi et al.*, 2000]. While the effects of inaccurate crustal models and noisy data are studied quite often, less attention is being paid to the resolution of the ill-conditioned problem, where even accurate structural models and noise-free data may provide a solution far from the true one [*Monelli and Mai*, 2008; *Page et al.*, 2009].

[3] In particular, *Olson and Apsel* [1982] studied the slip inversion of real data by means of singular value decomposition (SVD) assuming several types of inversion regularizations. The authors divided the inversion solution into two parts: stable and unstable. The stable part is demanded by the data, while the unstable part is unrecoverable by the data alone. Thus the key question, not discussed yet, is whether the stable part reflects at least the major features of the true (input) model. If not, the inversion is said to contain artifacts. Recently, *Zahradník and Gallovič* [2010] (hereinafter referred to as paper 1) attempted to understand some of the slip inversion artifacts. References to papers related to slip inversion are given by paper 1.

[4] In paper 1, seismograms for several rupture scenarios were forward simulated in a near-regional network of stations, which is also employed in the present paper (Figure 1). The resulting waveforms were inverted by two independent methods (one based on the conjugate gradient technique using back propagation of the waveform residuals [*Gallovič et al.*, 2009] and the other based on iterative deconvolution of point source contributions [*Sokos and Zahradník*, 2008]). The inversions yielded biased rupture speeds and, most interestingly, a strong spurious slip in the central part of the bilateral rupture model where there was almost no slip in the forward model. As a motivation the latter problem can also be illustrated by inverting the bilateral input model (Figure 2a) by yet another method, namely, the nonnegative least squares approach using the NNLS routine of *Lawson and Hanson* [1974]. Smoothing in both space and time is used; details are explained in section 2 and

[1]Department of Geophysics, Faculty of Mathematics and Physics, Charles University, Prague, Czech Republic.

0148-0227/11/2010JB007814

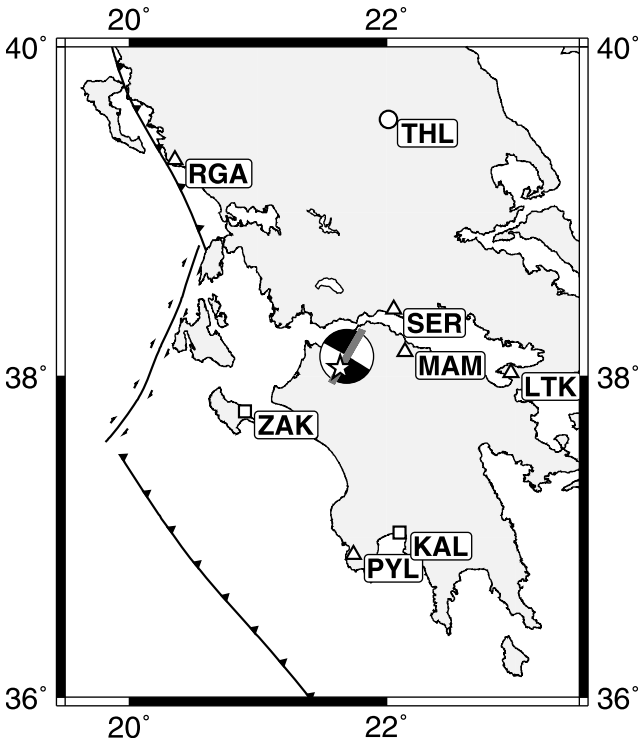

Figure 1. The Movri Mountain Mw 6.3 earthquake in Greece: the epicenter (asterisk), fault (gray bold line), focal mechanism (strike 30°, dip 87°, rake −178°) and eight near-regional stations are shown. This setup is used in this paper for inverting both synthetic and real data. The symbols refer to the station network: ITSAK (squares), NOA (circle), PSLNET (triangles). The main tectonic lines of western Greece are displayed.

in Text S1.[1] The result, presented in Figure 2b, also exhibits the persisting spurious asperity.

[5] In paper 1, the inversion behavior was analyzed by introducing so-called dynamic projection strips (DPSs). The DPSs were constructed by means of a "signal detector," a computation tool analyzing the correlation between complete observed waveforms and synthetics due to trial point sources. The strips were shown to be an extension of the projection line concept of seismic source tomography [*Ruff*, 1984; *Menke*, 1985]. They explain the role of the individual stations in the inversion, showing that the stations most constraining the inversion are those located along the fault direction. The DPS concept helped to explain the existence of the spurious asperity by combining the DPSs from all stations, giving rise to the so-called dark spot that also included the central part of the fault. As such, paper 1 represented an intuitive, physically based approach. The objective of the present paper is to complement it by a mathematically based approach.

[6] Since the forward problem under study is, in principle, linear, the inversion can be studied by the powerful technique of singular value decomposition, SVD [*Press et al.*, 1992; *Lawson and Hanson*, 1974]. Two factors restrict the applicability of the SVD technique in practice: (1) a large number of parameters, often technically prohibitive, (2) the need for nonlinear constraints, e.g., the slip positivity [*Olson and Apsel*, 1982; *Das et al.*, 1996], which are inapplicable in the SVD framework. Since the present paper aims at understanding the relations between mathematical and physical concepts, we can adopt simplifications to avoid these problems: a 1-D (line) source will keep the number of parameters low enough, and the main problems of slip inversions will be understandable even without the positivity constraint.

[7] The present paper shows how the above mentioned artifact (Figure 2b) can be explained by means of the SVD approach, which allows the separation of the stable and unstable parts of the solution. Furthermore, using SVD, we present a mathematical explanation of the DPSs and the dark spots and show how they control the inversion.

[8] The present paper has two parts. First, we explain the slip inversion procedure in terms of the well-known theoretical concepts of the SVD (linear algebra), such as singular vectors and regularization by means of truncation and smoothing. We also discuss the spatial-temporal complexity of the singular vectors to understand how to achieve balance between overregularized solutions (with possible artifacts), and underregularized solutions (vulnerable to data errors). Second, we apply the singular value analysis to the M6.3 earthquake, previously studied in paper 1. At the end we discuss that the features of the slip inversion procedure elucidated by the SVD are in the background of many slip inversion schemes, even those incorporating nonlinear

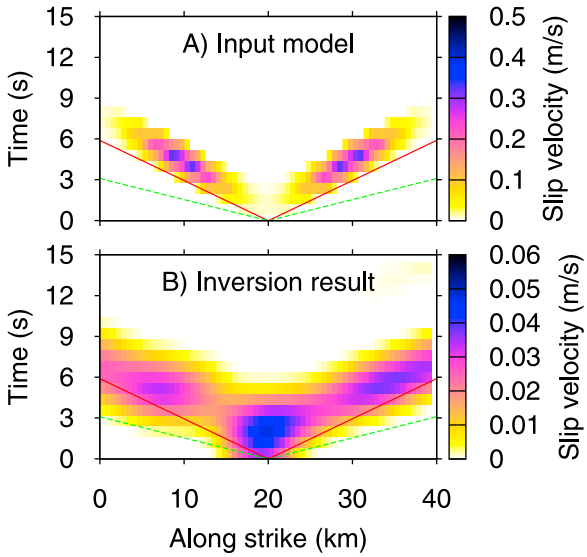

Figure 2. (a) Input slip velocity model for bilateral rupture propagation (prescribed source parameters). (b) Inversion result obtained by using the nonnegative least squares approach (NNLS). The solid red and dashed green lines correspond to S and P wave velocities at hypocentral depth, respectively. Note the disagreement of the major properties of the input and inverted source model, especially the spurious asperity in the center of the fault. A similar result is obtained even for other slip inversion methods (paper 1).

[1] Auxiliary materials are available in the HTML. doi:10.1029/2010JB007814.

constraints and those not explicitly working with singular vectors at all. We propose a procedure that should accompany detailed slip inversions to understand the role of the individual stations and to warn against potential drawbacks of the inversion.

2. Singular Value Analysis of Slip Inversion

2.1. Forward Problem

[9] The displacement wavefield u_j^s measured at station s, component j, is related to the earthquake slip velocity function $\Delta\dot{u}$ by means of the representation integral [*Aki and Richards*, 2002],

$$u_j^s(t) = \iint \Delta\dot{u}(x,\tau) H_j^s(x, t-\tau) dx d\tau, \tag{1}$$

where H_j^s are the displacement responses of the medium to excitation by a double-couple point source in space and step in time with unitary slip rate. After discretization of the spatial and temporal integrals, the representation theorem (1) can be expressed in matrix form:

$$\boldsymbol{u} = \mathbf{H}\boldsymbol{m}, \tag{2}$$

where vector $\boldsymbol{u}$ contains the displacement wavefields u_j^s of all stations and components considered, N elements in total; vector $\boldsymbol{m}$ encompasses M model parameters (samples of the slip velocity as a function of spatial coordinate and time). The two vectors are related to each other by matrix $\mathbf{H}$ [N rows × M columns], in which the jth column $\boldsymbol{H}(j)$ contains the impulse response due to the jth source position in space and time, $j = 1,\ldots, M$.

[10] We supplement (2) by a linear constraint on the scalar seismic moment M_0 that is assumed to be known in advance. It can simply be added to the matrix formulation (2),

$$\begin{pmatrix} L_u^{-1}\boldsymbol{u} \\ 1 \end{pmatrix} = \begin{pmatrix} L_u^{-1}\mathbf{H} \\ L_s^{-1}\boldsymbol{I} \end{pmatrix} \boldsymbol{m}, \tag{3}$$

or, in concise form,

$$\boldsymbol{d} = \mathbf{G}\boldsymbol{m}, \tag{4}$$

where $\boldsymbol{I}$ is a vector consisting of units, $L_u = \sqrt{\sum_{sij} u_{sij}^2}$ is the L2 norm of the data (i being the time index) and $L_s^{-1} = \mu\Delta S\Delta T/M_0$; μ is the rigidity of the medium, and ΔS and ΔT are the discretization elements of the fault area and the time interval, respectively. Note that the normalizing constants provide nondimensional data vector $\boldsymbol{d}$.

2.2. Inverse Problem

[11] If no additional constraints are added to the forward problem (4), it can be solved for $\boldsymbol{m}$ by the singular value decomposition (SVD) [e.g., *Press et al.*, 1992]. Matrix $\mathbf{G}$ can be uniquely decomposed into

$$\mathbf{G} = \mathbf{U}\Lambda\mathbf{V}^T, \tag{5}$$

where $\mathbf{U}$ [$N+1$, M] and $\mathbf{V}$ [M,M] are orthonormal matrixes ($\mathbf{U}^T\mathbf{U} = \mathbf{I}$, $\mathbf{V}^T\mathbf{V} = \mathbf{I}$) and Λ is a diagonal matrix consisting of singular values λ_i, $i = 1,\ldots, M$ (hereinafter assumed to be nonzero). Columns $\boldsymbol{V}_{(i)}$ of matrix $\mathbf{V}$ are so-called singular vectors. They are the eigenvectors of matrix $\mathbf{G}^T\mathbf{G}$ [M,M], forming an orthonormal basis system in the model parameter space. The $\mathbf{G}^T\mathbf{G}$ matrix contains the second derivatives of the L2 misfit with respect to the model parameters, the L2 misfit given by $1/2\|\boldsymbol{d} - \mathbf{G}\boldsymbol{m}\|^2$. The squares of singular values, λ_i^2, then represent the corresponding eigenvalues of matrix $\mathbf{G}^T\mathbf{G}$, expressing the sensitivity of the L2 misfit to changes of parameters $\boldsymbol{m}$ along the individual vectors $\boldsymbol{V}_{(i)}$. Columns $\boldsymbol{U}_{(i)}$ of matrix $\mathbf{U}$ are projections of basis vectors $\boldsymbol{V}_{(i)}$ into the data space (see equation (5)),

$$\boldsymbol{U}_{(i)} = \frac{\mathbf{G}\boldsymbol{V}_{(i)}}{\lambda_i}, \tag{6}$$

i.e., normalized seismograms related to the individual singular vectors. Being orthonormal in the data space, the $\boldsymbol{U}_{(i)}$ represent those eigenvectors of matrix $\mathbf{G}\mathbf{G}^T$[$N+1$,$N+1$] that correspond to its M nonzero eigenvalues.

[12] The Moore-Penrose pseudoinverse matrix of $\mathbf{G}$ can be expressed as

$$\tilde{\mathbf{G}} = \mathbf{V}\Lambda^{-1}\mathbf{U}^T. \tag{7}$$

The solution of the inverse problem, $\tilde{\boldsymbol{m}} = \tilde{\mathbf{G}}\boldsymbol{d}$, can thus be expressed as a linear combination of basis vectors $\boldsymbol{V}_{(i)}$,

$$\tilde{\boldsymbol{m}} = \sum_{i=1}^{M} \frac{\boldsymbol{U}_{(i)} \cdot \boldsymbol{d}}{\lambda_i} \boldsymbol{V}_{(i)}. \tag{8}$$

The $\boldsymbol{U}_{(i)}$ represent the vector basis in the M-dimensional data subspace that can be explained by the model parameters. The data vector in that subspace can be expressed as $\sum_{i=1}^{M}(\boldsymbol{U}_{(i)} \cdot \boldsymbol{d})\boldsymbol{U}_{(i)}$. The scalar product $\boldsymbol{U}_{(i)} \cdot \boldsymbol{d}$ can then be interpreted as a component of data vector $\boldsymbol{d}$ in the direction of basis vector $\boldsymbol{U}_{(i)}$. For the same reason, since $\boldsymbol{V}_{(i)}$ is the vector basis in the model space, ratio $(\boldsymbol{U}_{(i)} \cdot \boldsymbol{d})/\lambda_i$ represents the ith component of the parameter vector in the model space (see equation (8)). As such, equation (8) indicates that the data component = the parameter component times λ. Therefore, for a given change of a particular parameter component, a large or small λ yields a large or small change of the corresponding data component. Equally well, in case of inexact data (e.g., due to an inappropriate crustal model and/or additional noise), even a small error in a small data component can be amplified by the corresponding small λ to a large error in the respective parameter component. We further suppose that the singular vectors are sorted in descending order according to the size of their respective singular values λ.

[13] Putting (6) into (8), one obtains an alternative expression to that in (8),

$$\tilde{\boldsymbol{m}} = \sum_{i=1}^{M} \frac{\boldsymbol{V}_{(i)} \cdot \mathbf{G}^T\boldsymbol{d}}{\lambda_i^2} \boldsymbol{V}_{(i)} = \sum_{i=1}^{M} \frac{\boldsymbol{V}_{(i)} \cdot \tilde{\boldsymbol{c}}}{\lambda_i^2} \boldsymbol{V}_{(i)}, \tag{9}$$

where

$$\tilde{c}_i = \boldsymbol{G}_{(i)} \cdot \boldsymbol{d} = \frac{\boldsymbol{H}_{(i)} \cdot \mathrm{u}}{L_u^2} + \frac{1}{L_s}, \tag{10}$$

i.e., $\tilde{c}_i$ minus constant term $1/L_s$ is directly proportional to the scalar product of the impulse responses $\boldsymbol{H}(i)$ with data

vector $\boldsymbol{u}$. In this way, components of $\tilde{\boldsymbol{c}}$ are closely related to the correlations between the complete observed data $\boldsymbol{u}$ and "partial" synthetics $\boldsymbol{H}(i)$ corresponding to the individual point sources i with their respective location in time and space. Note the formal similarity between equations (8) and (9). While in the former equation the coefficients of the solution expansion are directly controlled by data vector $\boldsymbol{d}$, in the latter equation the data enter indirectly via $\mathbf{G}^T\boldsymbol{d} = \tilde{\boldsymbol{c}}$. Equation (9) suggests that the main role in the expansion to the first singular vectors is played by the similarity between them and $\tilde{\boldsymbol{c}}$. Any further features of the slip can only be obtained by employing singular vectors with smaller singular values. However, as already pointed out above, amplitudes of such singular vectors are more vulnerable to Green's function imperfections.

[14] Note that the interpretation of $\mathbf{G}^T$ d in terms of correlations (equation (10)) provides an alternative view of the least squares problem: fitting data $\boldsymbol{d}$ by parameters $\boldsymbol{m}$ ($\mathbf{G}\boldsymbol{m} = \boldsymbol{d}$, kernel $\mathbf{G}$) is substituted, via normal equations, by $\mathbf{G}^T\mathbf{G}\boldsymbol{m} = \mathbf{G}^T\boldsymbol{d} = \tilde{\boldsymbol{c}}$, i.e., by fitting correlations $\tilde{\boldsymbol{c}}$ by parameters $\boldsymbol{m}$, using kernel $\mathbf{G}^T\mathbf{G}$. Note that the definition of vector $\tilde{\boldsymbol{c}}$ is based on the same principle as the so-called "signal detector" of paper 1 (i.e., the correlations between the data and partial synthetics due to the individual point sources in the model space).

[15] As all singular values are sorted in descending order, the sum in equation (8) (or (9)) is typically not taken over the whole range M (total number of parameters) but only up to some $M' < M$, where λ (M') corresponds to the lowest singular value considered. The utilized singular vectors are termed the leading singular vectors. The idea is that (according to (8) or (9)) a given change in the parameter space in the direction $\boldsymbol{V}(i)$, associated with a small singular value $\lambda(i) < \lambda(M')$, yields a very small change in the data. Therefore, the effects of such small singular vectors can be suppressed. This is achieved by setting to zero all terms involving large values of $1/\lambda(i)$. Such an approach is practically useful since otherwise any small perturbation of $\boldsymbol{d}$ (e.g., due to noise, or due to imperfect knowledge of the propagating medium) yields a large change in $\boldsymbol{m}$, possibly driving the inversion to instabilities. Setting the coefficients of the solution expansion to zero for $\lambda(i) < \lambda(M')$ means that in the directions of the corresponding singular vectors $\boldsymbol{V}(i)$, the expansion coefficients are set to zero; this is one of the possible regularizations, and the resulting $\tilde{\boldsymbol{m}}$ is called the truncated solution. Other regularization approaches can be of course used. For example, regularization by adding linear smoothing constraints while keeping all singular vectors in the inversion. Similar and dissimilar effects of various regularizations are discussed further in the text and in Text S1.

2.3. Examples of Singular Vectors

[16] The singular vectors describe the slip inversion performance for a given fault position, distribution of stations and crustal structure. This information is independent of the specific parameters (the x-t rupture history) and data (seismograms) although, to be exact, matrix $\mathbf{G}$ is affected by the data through normalization constants L_u and L_s. However, they only serve to balance the weights of seismograms and the total seismic moment constraint. We show examples of singular vectors for a realistic configuration of a fault and near-regional stations, related to paper 1 (Figure 1). Matrix $\mathbf{G}$, containing the displacement impulse response of the medium (Green's functions and focal mechanism) is calculated by the discrete wave number method [*Bouchon*, 1981; *Coutant*, 1989] in a 1-D crustal model [*Haslinger et al.*, 1999] between 0.01 and 0.2 Hz. The source line depth is 17 km and the scalar seismic moment of the event is set to 3.4×10^{18} N m [*Gallovič et al.*, 2009]. We remind the reader that the shape of the singular vectors determines the final slip inversion solution (equation (8) or (9)) as these vectors form the basis system in the model space.

[17] Despite having eight stations in all at our disposal, in order to understand the individual role of the stations in the inversion, Figure 3 shows the singular vectors calculated assuming only single stations (namely, SER, ZAK, and RGA, see Figure 1 for their positions). The x and t components of the singular vectors are conveniently displayed in x-t diagrams. The vectors are sorted in descending order of their singular values. Although the singular vectors also include negative slip velocities (which is inevitable because the SVD approach cannot be combined with the positivity constraint), it does not preclude understanding the singular-vector properties. Indeed, for each of the three stations individually, the first singular vector (having the largest singular value $\lambda_{\max}$) has basically all components of the same size (say, a "homogeneous" vector). The other singular vectors are "inhomogeneous," taking the shapes of the inclined strips with angles depending on the station azimuths. The steepest strips of the opposite orientation characterize the singular vectors of the SER and ZAK stations. Contrarily, the strips associated with the RGA station are closer to horizontal. The strips illustrate that in the inversion each station contributes to the information about the model parameters mostly in a particular x-t direction. Note that the strips and angles characterizing the station singular vectors can be understood in terms of source tomography [*Ruff*, 1984; *Menke*, 1985; *Zahradník and Gallovič*, 2010]. The steepest angles are associated with the stations located in the along-strike directions and are given by the wave velocity of the dominating phase (i.e., Lg wave in our case of near-regional distances).

[18] The very simple monotonic character of the singular vectors of the individual stations suggests that combined information from more stations (most importantly from SER and ZAK) can help the inversion to locate the real slip x-t position. Therefore, Figure 4 shows the singular vectors as in Figure 3, but when all the eight stations are considered together. The first singular vector, associated with $\lambda_{\max}$, is again homogeneous. The next singular vectors up to $i = 5$ take the shape of elongated x-t patches because the inversion is dominated by the SER station (compare with the shape of the SER singular vectors in Figure 3). The dominance is due to the SER station's proximity to the fault, so that its amplitudes are significantly larger than those of the other stations. The next singular vectors are composed of still relatively large patches that have to be understood as combined information from all differently oriented strips found in the singular vectors of the individual stations (see Figure 3). These singular vectors will contribute to the inherent smoothness of the inverted truncated slip model (in terms of equation (8) or (9)) without any need of additional smoothing constraint (see also Text S1).

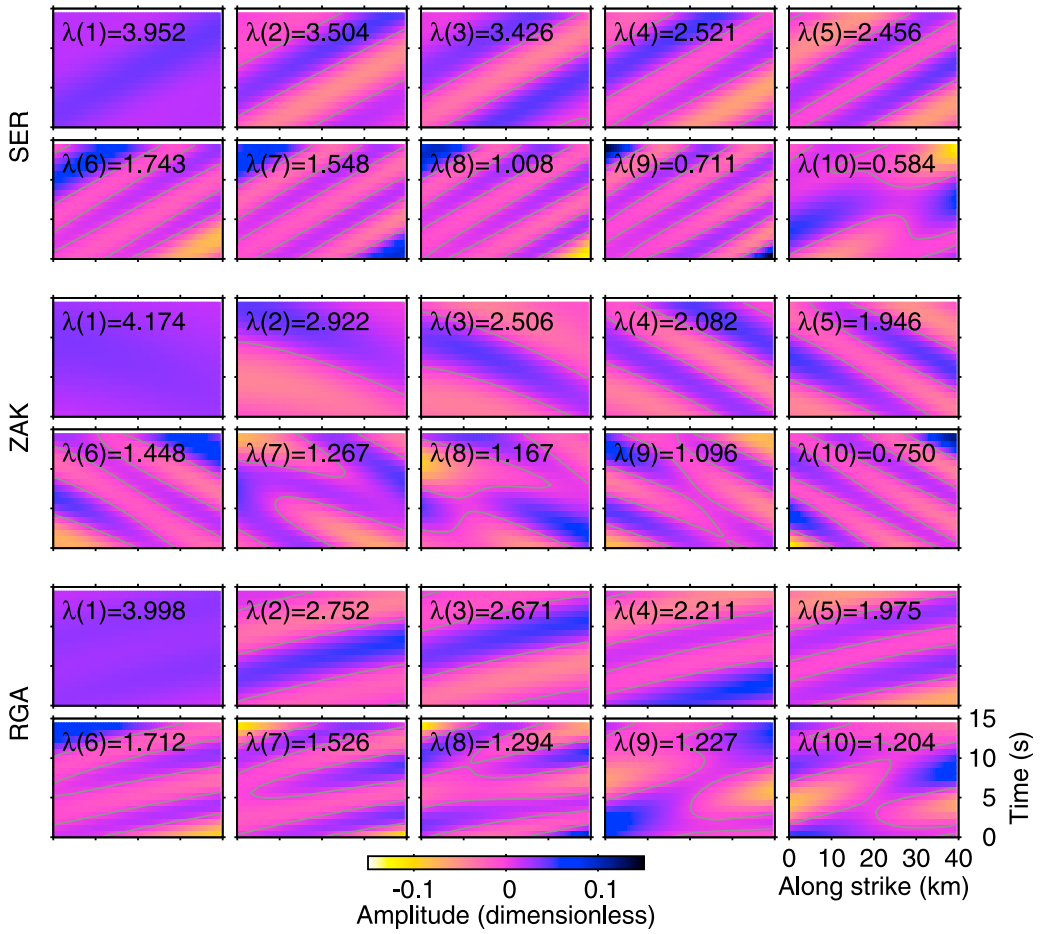

Figure 3. Leading singular vectors for a single-station linear problem of a line source in a 1-D crustal model. Each double row corresponds to one of the three selected stations (Figure 1). The spatial and temporal components of each singular vector are plotted against the horizontal and vertical axes, respectively; the size of the components is shown color coded. The values of the respective singular values λ are appended. Note the spatial-temporal complexity increasing with decreasing λ. The singular vectors depend on the assumed source and station positions and on the crustal structure.

[19] For larger i the singular vectors have more complex shapes, being increasingly more "oscillatory"; these are needed to reveal more detailed x-t structures in the slip model. However, as shown further, their proper combination might model not only small-scale, but also large-scale features of the slip pattern. For even smaller λ, the complexity of the singular vector increases up to "checkerboard" form.

[20] As stated above, the first singular vectors up to $i = 5$ in Figure 4 are dominated by the SER station. In Text S1 we show the singular vectors for the case when the station components are weighted according to the reciprocals of the seismogram L2 norms (thus weakening the role played by the SER station). Then, already the first singular vectors (up to $i = 5$) have the more complex shapes as for $i > 5$ in Figure 4. The explanation of how this can help in understanding the role of station weights in the inversion process is given in section 2.4.

2.4. Regularization (Synthetic Example)

[21] Now we use the singular vectors (examples are shown in Figures 3 and 4) to demonstrate how the slip inversion solution varies with different levels of truncation (zeroing contribution from singular vectors with small singular values). Figure 2a shows the synthetic input model considered. It corresponds to bilateral rupture propagation at constant speed, with two asperities located symmetrically on the fault to the northeast and southwest of the hypocenter (see the fault location in Figure 1). Note the almost zero slip in the center of the fault slip model.

[22] Figure 5 illustrates $\tilde{\boldsymbol{c}} = \mathbf{G}^T\boldsymbol{d}$ that is related to correlations between the data and impulse responses due to the individual sources at given x-t positions (see equation (10)). We remind the reader that $\tilde{\boldsymbol{c}}$ controls the contribution of the first leading singular vectors in the inversion solution expansion (see equation (9)). Figures 5a–5c assume only single stations used in the inversion (SER, ZAK, or RGA), while Figure 5d considers all eight stations together. Figures 5a–5c are dominated by strips of different angles. The strips show which of the point sources in the x-t space have their particular impulse responses correlated with the data vector. This closely relates the strips to the dynamic projection strips, introduced and discussed in paper 1. Figure 5d (employing all eight stations together) is related to the dark spot of paper 1. It is dominated by the northeastern

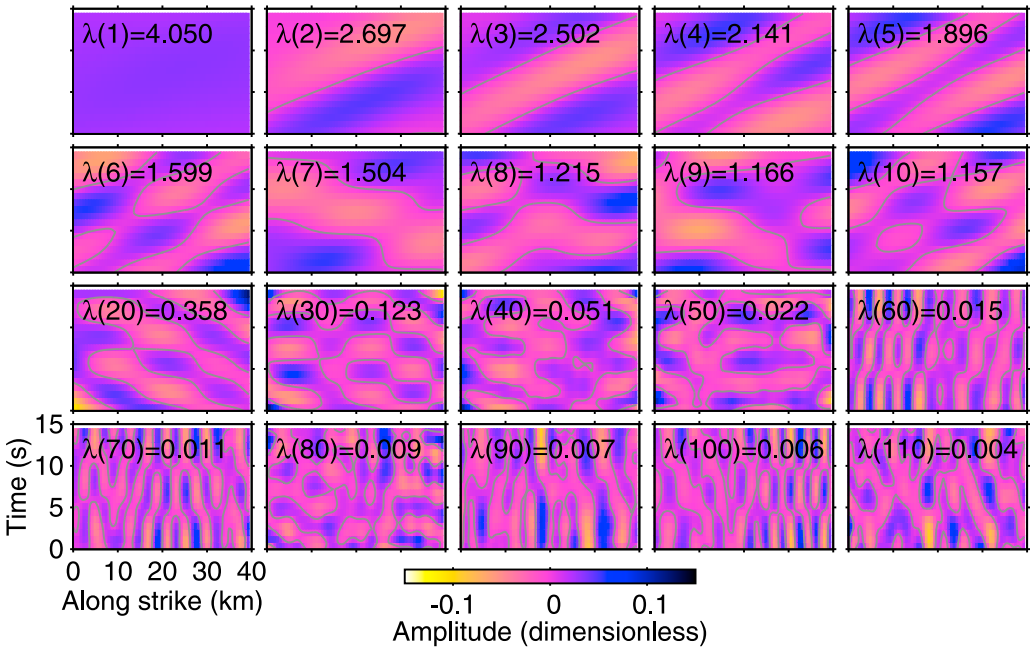

Figure 4. Singular vectors for the whole station network (Figure 1); the graphics are the same as in Figure 3. Comparison with the singular vectors of the single-station problems (Figure 3) shows that starting roughly at $\lambda(7)$, the singular vector pattern includes both "inclinations" typical of the individual stations. This property contributes to the resolution of the slip inversion. It is particularly important if the leading singular vectors already have this property (as in this case). Note that the shapes of the singular vectors (up to $i = 5$) are dominated by the SER station due to the proximity of this station to the source. In Text S1 we show the singular vectors for the case when the station components are weighted according to their L2 norm reciprocals. In such a case, the singular vectors take more complex shapes earlier. Note that the singular vectors with smaller singular values λ include a very complex pattern, theoretically being capable of providing details of the slip. However, their small λ reduces their practical use due to their high sensitivity to Green's function imperfections.

portion of the slip velocity, which is due to the proximity of the SER and MAM stations for which this part of the slip model is forward directive. Note that $\mathbf{G}^T\boldsymbol{d}$ has large amplitudes not only in the area of the existing slip (compare with Figure 2a) but also in the central part of the fault. In Text S1 we show this vector for the case when the station components are weighted according their respective L2 norm. In such a case, the SER and MAM stations are downweighted (due to their relative proximity to the fault) and the $\mathbf{G}^T\boldsymbol{d}$ plot is more symmetric, i.e., reflects the southwest asperity better, but still with a pronounced maximum in the central part of the fault.

[23] Now we evaluate the truncated solution (8) or, equivalently, (9) for the synthetic bilateral model. This can be done in two alternative ways:

[24] 1. The first way is to take the input model and multiply it by $\mathbf{G}$ to get synthetic data; these data can then be used in the inversion. Quantities $1/\lambda_i$ in (8) are set to zero beginning from a given $i = M'$ (as in the real data inversion).

[25] 2. Alternatively, start again from $\boldsymbol{m}$, now "skip" data $\boldsymbol{d}$ (not applicable in the real data inversion), and directly calculate the truncated solution as $\tilde{\boldsymbol{m}} = \mathbf{V}_p\mathbf{V}_p^T\boldsymbol{m} = \mathbf{R}\boldsymbol{m}$, where $\mathbf{V}_p$ is the matrix of singular vectors $\boldsymbol{V}(i)$ in columns with columns deleted beginning from $i = M'$. (The latter follows from substituting $\boldsymbol{d} = \mathbf{G}\boldsymbol{m}$ into the pseudoinverse problem $\tilde{\boldsymbol{m}} = \tilde{\boldsymbol{G}}\boldsymbol{d}$, obtaining $\tilde{\boldsymbol{m}} = \mathbf{V}\ \Lambda^{-1}\mathbf{U}^T\mathbf{U}\Lambda\mathbf{V}^T = \mathbf{V}_p\mathbf{V}_p^T\boldsymbol{m} = \mathbf{R}\boldsymbol{m}$.) Matrix $\mathbf{R}$ is called the resolution matrix. Comparing $\tilde{\boldsymbol{m}}$ with the given $\boldsymbol{m}$ provides important information about the inverse problem [*Lévêque et al.*, 1993].

[26] In some cases the resolution matrix itself can also be used to analyze trade-offs in the inverse problem. However, in our case it does not carry much useful information itself; it has almost constant diagonal elements (not shown here), suggesting the same trade-off for all points in the x-t plot.

[27] Figure 6 shows the inversion result for the synthetic example assuming various truncation levels and assuming either single stations in the inversion (SER, ZAK, RGA) or the complete set of eight stations. The regularization consists of removing (zeroing) singular vectors with singular values smaller than $\lambda_{\min}$, expressed as a fraction of $\lambda_{\max}$. Considering only the singular vectors with singular values larger than $\lambda_{\max}/5$ (Figure 6, first row), the resulting truncated slip image is relatively smooth, including also some negative values. When only one station is inverted, it retrieves the biased x-t slip pattern, controlled just by the corresponding singular vectors composed of the inclined strips (Figure 3). In particular, stations located approximately along the fault line (SER and ZAK) are able to recover only a part of the rupture that propagates in their directions because of the similarity between the singular vectors and the $\tilde{\boldsymbol{c}}$ plots (see equation (9)). The details of the rupture propagating away from the stations are hidden. All stations together yield a solution again similar to the $\tilde{\boldsymbol{c}}$ plot,

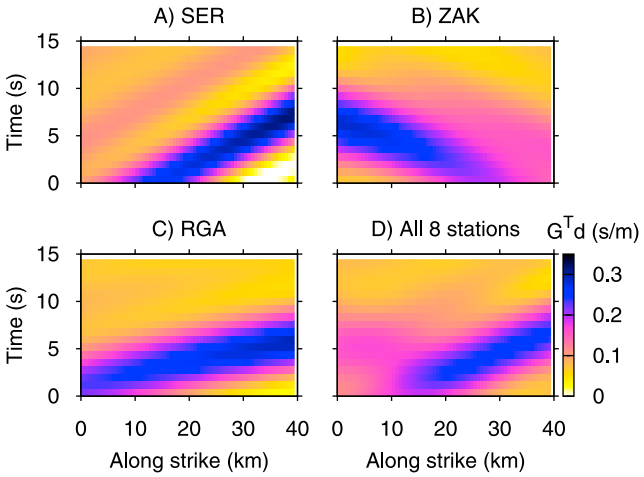

Figure 5. Analysis of the $\mathbf{G}^T\boldsymbol{d} = \tilde{\boldsymbol{c}}$ vector in the model space for the synthetic test (Figure 2a). The $\mathbf{G}^T\boldsymbol{d}$ components are proportional to the correlations between the complete seismograms (due to the finite extent source model) and the partial synthetics (due to single point sources at the individual x-t positions). (a-c) $\mathbf{G}^T\boldsymbol{d}$ for three single-station problems; (d) the whole network. The individual $\mathbf{G}^T\boldsymbol{d}$ vectors for each station are the mathematical counterpart of the dynamic projection strips of paper 1. They show what parts of the inversion solution are supported by each station for the specific input source model; see, for example, the narrow pattern of the $\mathbf{G}^T\boldsymbol{d}$ vector station SER due to the dominating forward directivity effect. Note that opposed to the singular vectors, the $\mathbf{G}^T\boldsymbol{d}$ vectors represent mixed information that is dependent not only on the stations but also on the slip model. However, since the information about the input model is transferred to the data, $\boldsymbol{d}$, the $\mathbf{G}^T\boldsymbol{d}$ vectors can be constructed also for the real data inversion, not only for synthetic tests. In Text S1 we show that in the case of station components weighted according to their respective L2 norm, the $\mathbf{G}^T\boldsymbol{d}$ vector for all stations has a more symmetric character, not being dominated by the proximity of station SER to the fault.

providing larger slip velocity values in the direction of the (closest) SER station.

[28] If more singular vectors are kept in the SVD solution ($\lambda_{min} = \lambda_{max}/10$ and $\lambda_{max}/100$, Figure 6, middle rows), the individual stations are able to recover gradually more details about the part of the rupture propagating away from them. The inversion employing all stations together also performs better; that is, it clearly shows the bilateral character of the rupture. However, the all-station inversion yields an asperity located in the center of the fault, where there is almost no slip in the input model (see Figure 2). We call this feature the "false asperity," or "artifact." Note that the (synthetic) data are fitted almost perfectly, with the variance reduction larger than 0.99. In paper 1 the same artifact was studied by two independent inversion methods, shown as an extremely stable persisting feature; this was explained in paper 1 by means of the dynamic projection strips. Here it is shown to have its equivalent mathematical explanation in terms of the truncated solution.

[29] Figure 6 (fourth row) shows the inversion result for an extreme case of the $\lambda_{min} = \lambda_{max}/1000$. In this case even the single-station inversion indicates the bilateral character of the input model. If we further add more singular vectors, we could, in principle, resolve the input model exactly (as none of the equations in the forward problem are linearly dependent). This is so thanks to the increased space-time complexity of the single-station singular vectors that are, however, associated with very small singular values. This makes their contribution to the solution vector very vulnerable to data errors and Green's function imperfections, thus inapplicable in real applications.

[30] This above explained study of the regularization by means of the solution truncation is supplemented by the case of the weighted synthetics in the inverse problem, presented in Figure S8 in Text S1. The regularization behaves analogously. The most regularized solutions ($\lambda_{min} = \lambda_{max}/5$) are similar to the $\mathbf{G}^T\boldsymbol{d}$ plots that due to the downweighted SER station, already indicate the bilateral character of the rupture (Figure S7a). However, the spurious central asperity is even stronger.

[31] In Text S1 we also present the results for another type of regularization based on space-time smoothing, utilizing both SVD and nonnegative least squares approaches (NNLS) to invert the synthetic waveforms (see also Figure 2b). Again, the spurious asperity is present. We interpret the existence of such an artifact common to different methods as follows. Despite the regularization used, the problem to be solved shares some common features with the nonregularized (original) inverse problem. Among the most important are combinations of model parameters that most affect the comparison of seismograms (i.e., singular vectors with large singular values), and an "extended" null space (i.e., unstable part of the solution composed of singular vectors with singular values close to zero). The aim of any inversion approach is to obtain as good fit with the data as possible, providing a stable solution. Clearly, the stable part of the solution is related to the singular vectors with the largest singular values. Various methods approach the search for the stable solution in different ways. The SVD truncation eliminates the extended null space singular vectors from the solution. The smoothing constraint preserves the already smooth singular vectors because they are able to fit the seismogram part of the data vector efficiently, while it modifies the other singular vectors to fit the smoothing equations. Iterative inverse solvers (iterative deconvolution and the conjugate gradient approaches from paper 1) follow the steepest descent of the misfit, which is again given by the first singular vectors. This interpretation suggests that many methods (even those not explicitly working with the singular vectors) might provide such a biased result.

3. Application to Real Data

[32] The application is shown for the Movri Mountain earthquake, analyzed in paper 1 [see also *Gallovič et al.*, 2009; *Konstantinou et al.*, 2009; *Cesca et al.*, 2010]. Here we reconsider the problem within the framework of the regularized SVD technique. The singular vectors, in which the inverse solution is expanded, are the same as before (Figures 3 and 4). Figures 7a–7c show $\tilde{\boldsymbol{c}}$ for stations SER, ZAK, RGA, similar to the synthetic case in Figures 5a–5c. The narrow strip at SER and the broad strip at ZAK suggest the predominance of a unilateral rupture, as explained in

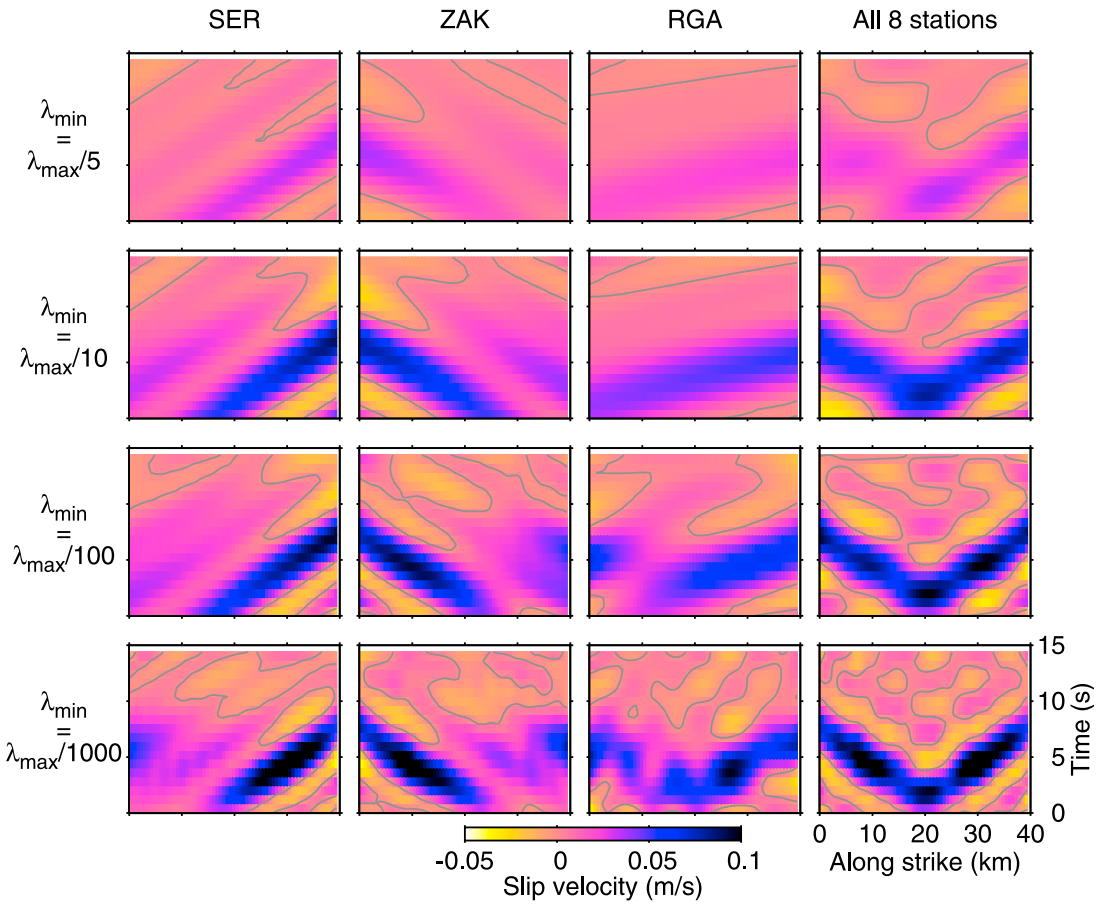

Figure 6. The truncated solutions of the slip inversion problem for the synthetic bilateral model (Figure 2a) assuming single stations (first to third columns) and the whole station network (fourth column). The x-t pattern of the inverted slip velocity model is color coded. The four rows correspond to various levels of the solution truncation, performed by zeroing singular vectors with λ smaller than given λ_{min} (see legend). The eight-station solutions in the first to third rows are characterized by an artifact, a spurious slip not existing in the input model. It is clearly demonstrated that the dominant combined effect of stations SER and ZAK, situated almost in the direction of the fault, yields the artifact. Only the weakly regularized solution (bottom right) is less affected by the artifact. Nevertheless, in practice, inevitable data errors and Green's functions imperfections prohibit the use of the weak stabilization. The artifacts cannot be easily detected since the data are fitted almost perfectly already for the first row, with a variance reduction of 0.997. Note the similarity between the strongly regularized solutions (first row) and the $\mathbf{G}^T\boldsymbol{d}$ vectors in Figure 5 (see explanation in text). Text S1 shows similar results when station weighting is considered.

paper 1. Figure 7d shows the $\tilde{\boldsymbol{c}}$ plot for the whole station network that further confirms the predominant rupture propagation. In Text S1, Figure S7b is an alternative for the case of weights applied to the station components. Figure S7b is less dominated by the unilateral trend as the closest station (SER) is downweighted with respect to the rest of the stations.

[33] Regarding the inversion, we use equation (8) (or, equivalently, equation (9)) directly employing the real data; the resolution matrix framework cannot be used as in the synthetic data case because the input model is not known. The sum in (8) or (9) is again calculated up to a given singular value λ_{min}, specified by a fraction of the maximum singular value λ_{max}. The truncated solutions for various λ_{min} employing either a single station or all stations are shown in Figure 8. In Text S1 we also present an analogous test for the case of the applied station component weights (Figure S9). Figure 8 (first and second rows) is for λ_{min} equal to $\lambda_{max}/3$ and $\lambda_{max}/5$. All the SVD solutions (both for the individual stations and all stations together) resemble the strips of $\mathbf{G}^T\boldsymbol{d}$ in Figure 7. This means that up to approximately $\lambda_{max}/5$ only the singular vectors having the highest correlation with $\tilde{\boldsymbol{c}}$ (see equation (9)) form the solution. In this way, one can already estimate from the $\mathbf{G}^T\boldsymbol{d}$ plot that the rupture predominantly propagated toward station SER. On the contrary, both $\mathbf{G}^T\boldsymbol{d}$ and the slip inversion for the ZAK station features a broader strip, separated into two substrips, suggesting two asperities. When all the stations are considered together, the unilateral rupture direction is further supported (even if the station weights are considered, see Figure S9 in Text S1).

[34] Assuming more singular vectors (up to $\lambda_{max}/9$) in the truncated solution, one can see that the coherent smooth

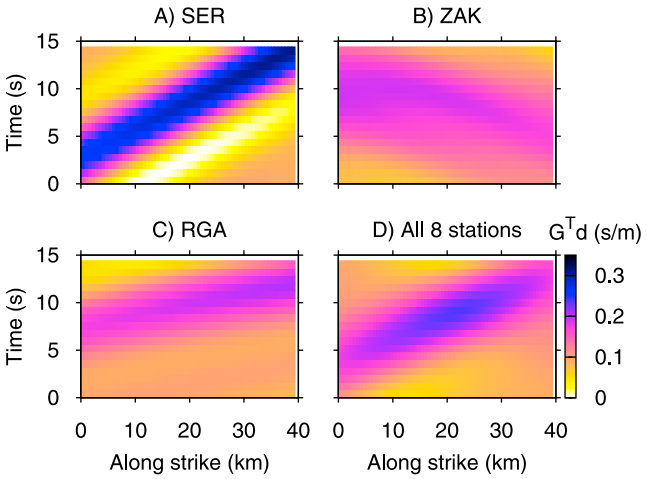

Figure 7. (a-c) The $\mathbf{G}^T\boldsymbol{d} = \tilde{\boldsymbol{c}}$ vectors as in Figure 5, but here for the real case of the Movri Mountain earthquake. (d) The mathematical counterpart of the dark spot in paper 1 is a bound within which the strongly regularized solutions will appear. The variability of the less regularized inversion results (Figure 8) will be determined by the complexity of the added singular vectors. The $\mathbf{G}^T\boldsymbol{d}$ vector for the weighted station components case is shown in Text S1; in that case the vector is less affected by station SER.

positive slip velocity areas split up (Figure 8), while the rest of the image starts being characterized by a larger amount of negative values. One can also see that the fit with the data in terms of variance reduction does not change much, from 0.679 for $\lambda_{min} = \lambda_{max}/3$ to 0.707 for $\lambda_{max}/9$. The slip velocity images for the minimum singular value smaller than $\lambda_{max}/20$ are already greatly distorted, having also large patches of negative values. This is so because the less constrained singular vectors, more vulnerable to imperfections in the synthetic Green's functions, already spoil the solution. Note that adding more singular vectors in the solution expansion cannot help as the associated errors would only be larger.

[35] To summarize, using only a few leading singular vectors, we arrive at a simple smooth model, moreover, controlled by $\mathbf{G}^T\boldsymbol{d}$. Further details are extremely vulnerable to data imperfections in terms of noise and/or improper crustal model, and thus depend on the minimization approach taken. A good example of such an uncertain detail is the indication of partial rupture propagation to the southwest (from 10 to 0 km, between 5 and 10 s). It is expressed by a larger slip velocity patch in Figure 8 (bottom right) (or, better, for the case of applied weights in Text S1 in Figure S9, $\lambda_{min} = 1/7 \ldots 1/20\lambda_{max}$). Note that the possibly asymmetric bilateral character of the rupture was suggested by other authors [*Konstantinou et al.*, 2009; *Cesca et al.*, 2010]. Our study seems to explain their finding but, at same time, warns that this might only be an artifact of the regularized solution. Similarly, the present study suggests that the split of the main asperity in space and time for the Movri Mountain earthquake obtained by the conjugate gradient technique [*Gallovič et al.*, 2009] and the equivalent solutions presented in Figure 11 of paper 1 have to be understood in the same way.

[36] Text S1 illustrates that the smoothing and/or using the NNLS approach does not help us to decide whether the Movri Mountain earthquake was an asymmetric bilateral rupture, or a predominantly unilateral rupture with a delayed central asperity. More details of the source model can be investigated only by supplementing the inversion by additional data (such as strong motion records, GPS) or additional constraints, such as hypocenter location, constant rupture velocity, etc. [*Dreger and Kaverina*, 2000]. However, as the data are insensitive to further details of the slip model, the (often uncertain) constraints would take over the inversion and the "refined" slip image would be determined by the constraints themselves. This limitation has not yet been broadly recognized in practical slip inversions.

4. Discussion and Conclusions

[37] The linear slip inversion is an unstable problem. Typically, it is stabilized by supplementing nonlinear constraints, such as positivity and/or spatial-temporal smoothing. This paper shows that many features of the slip inversion can already be understood in the linear formulation, i.e., where the singular value decomposition (SVD) is applicable. The SVD technique enables understanding issues such as instability, smoothing, trade-off and artifacts.

[38] The SVD creates a basis system in the model space in terms of the eigenvectors of matrix $\mathbf{G}^T\mathbf{G}$ (also called singular vectors). Each singular vector is supplemented by its singular value λ expressing the sensitivity of the data to changes along the corresponding singular vector in the model space. The inverse solution can be expressed as a sum of the singular vectors with weights proportional to the reciprocal of the singular values (equations (8) and (9)). We assume that the singular vectors are sorted according to their respective singular values in descending order. Starting with the analysis of singular vectors for individual stations, the first singular vectors are shown to have the character of smooth inclined strips with angles given by the station azimuths with respect to the fault strike. When the whole station network is considered, more complex shapes appear, being combination of the individual station strips. Such a "low-frequency" character of the singular vectors is an advantage because, typically, synthetic Green's functions perform better in the low-frequency band. The singular vectors with lower data sensitivity (small λ) have more complex ("high-frequency") shapes, being more vulnerable to Green's function imperfections and/or noise in the data.

[39] The slip inversion is first studied on a synthetic example of a symmetric bilateral rupture. It is shown that the slip model expansion into the first singular vectors is driven by $\tilde{\boldsymbol{c}} = \mathbf{G}^T\boldsymbol{d}$. This quantity is closely related to the so-called dynamic projection strips (DPSs) introduced in paper 1 as an extension of the projection line concept of seismic source tomography. DPSs were intended as a practical tool to identify the individual station contributions to the slip inversion, constructed by means of the "signal detector," i.e., a computational tool analyzing the correlation between complete observed waveforms and partial synthetics due to trial point sources. The present paper provides a mathematical explanation why the DPSs (i.e., $\tilde{\boldsymbol{c}} = \mathbf{G}^T\boldsymbol{d}$) control the inversion.

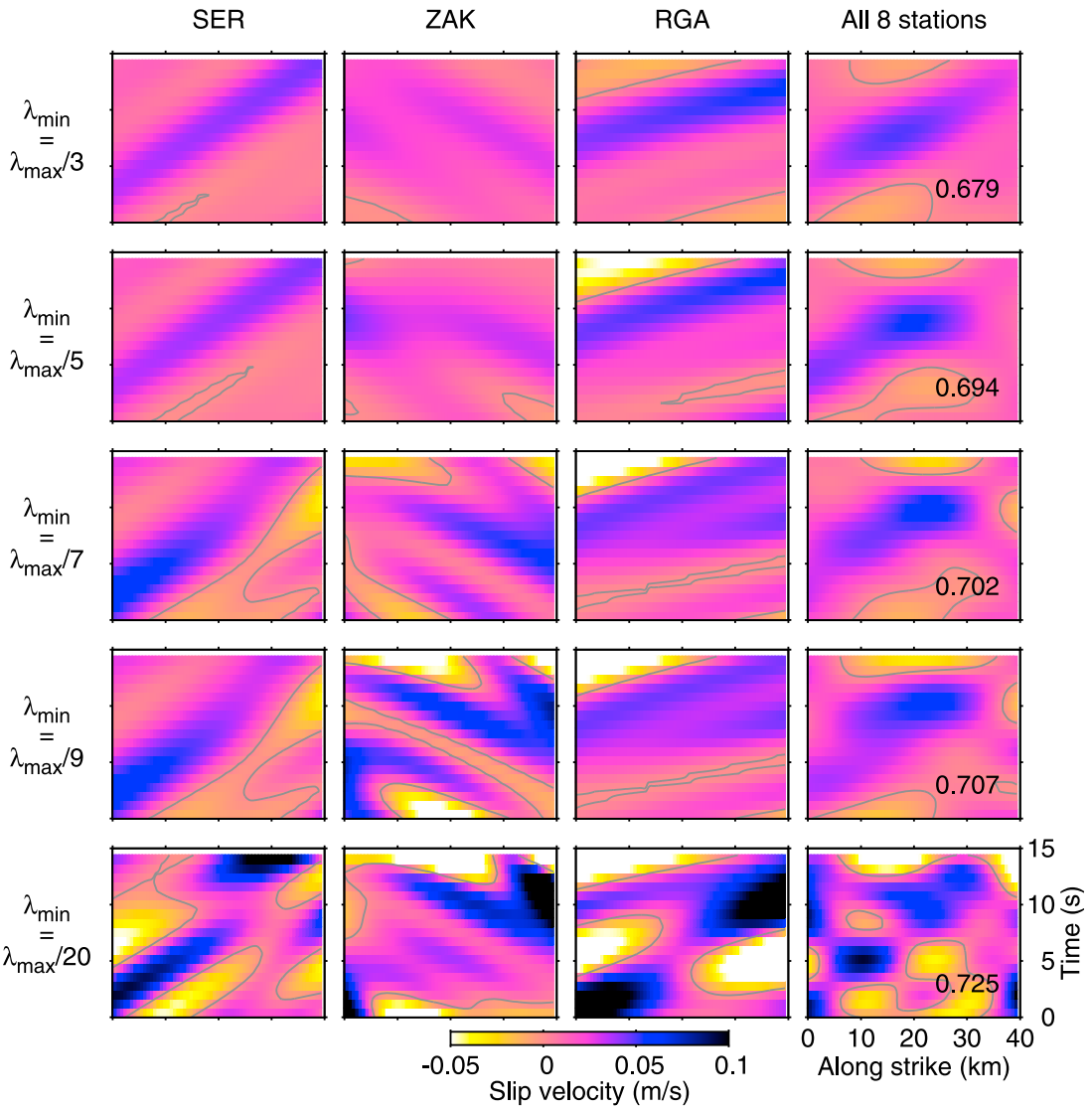

Figure 8. The truncated solutions (the slip velocity pattern) as in Figure 6 but here for the real case of the Movri Mountain earthquake. According to equation (9), the $\mathbf{G}^T\boldsymbol{d}$ vector of Figure 7, combined with progressively more complex singular vectors (i.e., with decreasing λ), increases the complexity of the slip model. Note that the slip velocity model in the fifth row (with the saturated color scale) is largely distorted. Adding more singular vectors would result in a completely "random" (unphysical) pattern due to the imperfections of the Green's functions employed. The numbers in the fourth column are the respective variance reductions. In Text S1 we show analogous results for the case of the weighting of the station components. That case (when the forward directive station SER is downweighted) weakly indicates a possibility of the rupture propagation also in the opposite direction (from 10 km at 5 s to 0 km at 8 s).

[40] When inverting waveforms for the slip velocity image, the sum over singular vectors is truncated, preserving only the so-called leading singular vectors. Keeping only a few leading singular vectors works seemingly as smoothing due to the smooth character of the singular vectors themselves. However, such regularizations (although providing a stable solution) may also have a negative effect on the inversion. For example, a symmetric bilateral rupture with a small amount of slip at the hypocenter is erroneously imaged as having a strong asperity at the hypocenter. Thus, the truncated solution not only limits the resolution, but in some problems even simple and stable structures in the parameter space may differ from the true ones. Note that this does not mean that the stable structures are incorrect. It is a correct part of the solution of the inverse problem, however, it is an incomplete representation (approximation) of the true solution.

[41] The spurious asperity artifact was previously described in paper 1, using two other inversion approaches including nonlinear constraints of positivity. In paper 1 the artifact was explained in terms of the DPSs. Here we interpret the effect as follows: The data fitting procedure implicitly starts by changing the parameters related to the largest singular values as they control the data fit most efficiently. This represents a stable part of the inverse problem. The inversion techniques then "move" along the

poorly constrained singular vectors. This is the unstable part, sensitive to inappropriate crustal models, noise in the data and the particular inversion approach, providing different (biased) details for different inversions. However, as shown in section 2.4, the dangerous artifacts may already arise in the most stable part, related to the largest singular values, when the singular vectors of small singular values are discarded from the solution.

[42] This is the reason why such artifacts are very persistent and difficult to recognize and/or remove. They are common to many inversion methods including those not explicitly working with the singular vectors at all. For example, Text S1 shows that for reasonable choices of the weight of the smoothing constraint in the inversion results in the same artifact as above even if the nonnegativity constraint is applied (see also Figure 2b). This is so because the first singular vectors are both smooth and also able to fit the seismogram part of the data, thus they are inverted as if without the smoothing constraint. The other singular vectors are modified and then used in the inversion to satisfy the smoothing equations only (having a small effect on the seismogram fit).

[43] Besides the slip artifact, the synthetic tests of paper 1 revealed a biased rupture velocity common to independent methods, mainly in the bilateral rupture model. The biased velocity can also be explained in terms of the solution truncation; the apparent rupture velocity is given predominantly by the inclined strips of the leading singular vectors controlled by the individual stations. That bias, common to different methods, is again nothing but the stable (although incomplete) part of the solution caused by the dominance of the leading singular vectors.

[44] By incrementally adding more singular vectors in the inversion of the synthetic example, the truncated solution is brought closer to the correct solution (i.e., removing the artifacts). In practice, however, as shown on the real near-regional data of the Movri Mountain earthquake, this is not practically feasible and regularization is unavoidable; the synthetic Green's functions deviate from the real ones, data contain noise; hence underregularized solutions are vulnerable to errors. In such a case the inversion would be unstable, clearly yielding unphysical source models. Therefore, the use of only a small number of singular vectors is inevitable. The opposite effect, i.e., the poor resolution of the overregularized solutions, is well known: the resulting slip pattern has no details; it is formed by a single patch or a few large patches. This paper paid attention to an additional (although related) issue that even the overregularized solution might contain artifacts and biases due to incomplete representation of the source model. This is an important practical warning against misinterpretation of stable features that look physically reasonable, but deviate from the true slip. Another lesson learned in this paper is a warning against checking resolution with a synthetic model similar to that one derived during the inversion of real data [see also *Lévêque et al.*, 1993]. Indeed, as the inverted model is already well represented by the leading singular vectors (even if the true slip is not), a synthetic test employing the same set of singular vectors will return the same model. Such result might be wrongly interpreted as a validation of the inverted image.

[45] In the presented example only the frequency range up to 0.2 Hz was considered. It is, therefore, important to discuss what happens when one uses a broader frequency range in the inversion (e.g., up to 1 Hz) and the same near-regional data. Again, as the singular values decrease, the singular vectors appear more and more similar to checkerboards. In the x-t plots, the size of the single cells can be related to a characteristic frequency and a characteristic wave number, which both generally increase as the singular values decrease. The leading singular vectors for the individual stations again have the strip character. However, in the case of considering the frequency range up to 1 Hz, the strips range from broad (such as those for $f < 0.2$ Hz) to very narrow ones. Furthermore, the associated singular values decay less quickly, thus with the same threshold $\lambda(M')$ we use a larger number of singular vectors, $M'' > M'$. Not surprisingly, when the associated singular vectors are employed in the inversion of synthetic data, the resulting slip image is sharper, reflecting the use of singular vectors with narrow strips. On the other hand, when the same singular vectors are used to invert real data, the resulting slip image does not change much (compared to $f < 0.2$ Hz). This can be explained by the effect of $\boldsymbol{U}(i) \cdot \boldsymbol{d}$ in the truncated solution sum (equation (8)). Indeed, the normalized seismograms $\boldsymbol{U}(i)$ (see equation (6)) corresponding to the singular vectors characterized by narrow strips are of a high-frequency character, and due to the crustal model imperfections, the scalar product of $\boldsymbol{U}(i)$ with the data vector d is very low, i.e., the contribution of such a singular vector in the inversion is "negligible." Note that this is not the case for the "high-frequency" singular vectors with low singular values ($>M''$) because although their $\boldsymbol{U}(i) \cdot \boldsymbol{d}$ are again low, the incorrect values of $\boldsymbol{U}(i) \cdot \boldsymbol{d}$ are amplified by the large reciprocal of their small singular values (see equation (8)), so these produce a kind of instable "high-frequency noise" in the inverted slip image. To conclude, the instabilities of the inversion take place, from the perspective of the linear SVD inversion, when taking into account singular vectors of small singular values with high-frequency $\boldsymbol{U}(i)$ being incorrect due to improper Green's functions, independently of the frequency range considered.

[46] Smooth model controlled only by the leading singular vectors (and by the $\tilde{\boldsymbol{c}}$ vector) can be inferred. Nevertheless, when properly understood, it already provides valuable information about the major features of the slip process. It bears an important piece of information about the predominant rupture direction, a possible delay of the major slip process with respect to origin time, etc. However, the proper understanding of the roles of the individual stations, possible biases, artifacts, and tradeoffs is required. This can be gained from parallel studies of the singular vectors of the inversion problem for a station network and for a suite of single-station problems. The highly regularized model can be understood as an important intermediate step between the centroid determination and a more advanced slip inversion. In the advanced slip inversion one can add additional data, e.g., strong motion records and/or GPS [*Page et al.*, 2009], which help correct biases in the slip model. If additional data are not available, physical constraints such as the hypocentral position and rupture velocity can be added, typically making the inversion nonlinear [*Dreger and Kaverina*, 2000]. However, one has to bear in mind that the resulting

finer details of the solution might then be forced by the constraints themselves, not always being sufficiently dictated by the data (i.e., being only allowed by them). Indeed, incorrect constraints (e.g., inaccurate hypocenter position) might bias the slip inversion, too.

[47] To give an example of how the singular vector analysis can be used to anticipate possible bias due to improper station coverage (e.g., the bias of the rupture speed and/or the presence of artifacts), let us discuss the role of station weights in the inversion. Nearby stations are typically characterized by larger amplitudes than the more distant stations. This causes the first leading singular vectors (for the whole station network) to be composed of those associated with the nearest station considered (SER in our case). This can be called implicit weighting. Thus, the inversion tends to first fit this station, which, however, leads to a bias of the inverted model (unilateral rupture propagation toward SER, see Figure 6, first row) because the problem is similar to a single-station inversion. Contrarily, weakening the SER station effect in the inversion (as in Text S1) leads to a less biased result (Figure S8) because now the leading singular vectors already contain information even from stations lying in the opposite direction from the fault. From a practical point of view, this only warns against implicit weighting in the inversion, which can bias the solution considerably. Therefore, at least some down-weighting of the closest station is always desirable. Of course, station weighting has to be done cautiously to avoid enhancing distant stations with less constrained Green's functions too much.

[48] Another example refers to the issue of improper azimuthal coverage. Figure 3 indicates that for example, if all stations had a similar azimuth, the singular vectors would all be elongated in the same direction. The patches would then not arise, x would strongly tradeoff with t, and the finite x-t structures could not be resolved. In simple words, the performance of the inversion depends on how well can the true slip distribution be expanded into the first eigenvectors of $\mathbf{G}^T\mathbf{G}$. Interpreters have to be aware of the spurious effects that might appear, as they are difficult to detect in the results. The bias caused can be learned from SVD and/or dynamic projection strip analysis of the synthetic inversion tests.

[49] Finally, let us emphasize again that all the ideas about singular vectors and their roles in the inversion are valid for many inversion schemes, i.e., even those that do not explicitly work with the singular vectors at all. We also point out that our discussion is not to be generalized to all types of artifacts. Here we have discussed only artifacts common to several inversion methods. Different regularization methods may yield additional different artifacts. However, as they differ across the methods, they are less dangerous, being easier to recognize.

[50] **Acknowledgments.** The authors greatly appreciate the free Internet access of waveforms provided by NOA (THL) and ITSAK (stations ZAK, KAL). The remaining stations (RGA, MAM, SER, LTK, PYL) belong to the PSLNET network, cooperated by the Charles University. We thank G. Festa and an anonymous reviewer for their valuable comments that significantly improved the manuscript. Financial support from GAUK14509, GACR 205/08/P013 and 210/11/0854, MSM0021620860.

References

Aki, K., and P. G. Richards (2002), *Quantitative Seismology*, Univ. Sci., Sausalito, Calif.

Bouchon, M. (1981), A simple method to calculate Green's functions for elastic layered media, *Bull. Seismol. Soc. Am.*, *71*, 959–971.

Cesca, S., S. Heimann, and T. Dahm (2010), Rapid directivity detection by azimuthal amplitude spectra inversion, *J. Seismol.*, *15*, 147–164, doi:10.1007/s10950-010-9217-4.

Coutant, O. (1989), Program of numerical simulation AXITRA, research report, Lab. de Geophys. Interne et Tectonophys., Grenoble, France.

Das, S., R. Suhadolc, and B. V. Kostrov (1996), Realistic inversions to obtain gross properties of the earthquake faulting process, *Tectonophysics*, *261*, 165–177.

Dreger, D., and A. Kaverina (2000), Seismic remote sensing for the earthquake source process and near-source strong shaking: A case study of the October 16, 1999 Hector Mine earthquake, *Geophys. Res. Lett.*, *27*, 1941–1944.

Gallovič, F., J. Zahradník, D. Křížová, V. Plicka, E. Sokos, A. Serpetsidaki, and G-A. Tselentis (2009), From earthquake centroid to spatial-temporal rupture evolution: Mw 6.3 Movri Mountain earthquake, June 8, 2008, Greece, *Geophys. Res. Lett.*, *36*, L21310, doi:10.1029/2009GL040283.

Hartzell, S. H., and T. H. Heaton (1983), Inversion of strong ground motion and teleseismic waveform data for the fault rupture history of the 1979 Imperial Valley, California earthquake, *Bull. Seismol. Soc. Am.*, *73*, 1553–1583.

Haslinger, F., E. Kissling, J. Ansorge, D. Hatzfeld, E. Papadimitriou, V. Karakostas, K. Makropoulos, H.-G. Kahle, and Y. Peter (1999), 3D crustal structure from local earthquake tomography around the Gulf of Arta (Ionian region, NW Greece), *Tectonophysics*, *304*, 201–218.

Konstantinou, K. I., N. S. Melis, S.-J. Lee, C. P. Evangelidis, and K. Boukouras (2009), Rupture process and aftershocks relocation of the 8 June 2008 Mw 6.4 earthquake in northwest Peloponnese, western Greece, *Bull. Seismol. Soc. Am.*, *99*, 3374–3389.

Lawson, C. L., and R. J. Hanson (1974), *Solving Least Square Problems*, 340 pp., Prentice-Hall, Englewood Cliffs, N. J.

Lévêque, J.-J., L. Rivera, and G. Wittlinger (1993), On the use of the checker-board test to assess the resolution of tomographic inversions, *Geophys. J. Int.*, *115*, 313–318.

Menke, W. (1985), Imaging fault slip using teleseismic waveforms: Analysis of a typical incomplete tomography problem, *Geophys. J. R. Astron. Soc.*, *81*, 197–204.

Monelli, D., and P. M. Mai (2008), Bayesian inference of kinematic earthquake rupture parameters through fitting of strong motion data, *Geophys. J. Int.*, *173*, 220–232.

Olson, A. H., and R. J. Apsel (1982), Finite faults and inverse theory with applications to the 1979 Imperial Valley earthquake, *Bull. Seismol. Soc. Am.*, *72*, 1969–2001.

Page, M. T., S. Custódio, R. J. Archuleta, and J. M. Carlson (2009), Constraining earthquake source inversions with GPS data: 1. Resolution-based removal of artifacts, *J. Geophys. Res.*, *114*, B01314, doi:10.1029/2007JB005449.

Press, W. H., B. P. Flannery, S. A. Teukolsky, and W. T. Vetterling (1992), *Numerical Recipes in Fortran, The Art of Scientific Computing*, 2nd ed., Cambridge Univ. Press, New York.

Ruff, L. J. (1984), Tomographic imaging of the earthquake rupture process, *Geophys. Res. Lett.*, *11*, 629–632.

Sekiguchi, H., K. Irikura, and T. Iwata (2000), Fault geometry at the rupture termination of the 1995 Hyogo-ken Nanbu earthquake, *Bull. Seismol. Soc. Am.*, *90*, 117–133.

Sokos, E., and J. Zahradník (2008), ISOLA A FORTRAN code and a Matlab GUI to perform multiple-point source inversion of seismic data, *Comput. Geosci.*, *34*, 967–977.

Zahradník, J., and F. Gallovič (2010), Toward understanding slip inversion uncertainty and artifacts, *J. Geophys. Res.*, *115*, B09310, doi:10.1029/2010JB007414.

F. Gallovič and J. Zahradník, Department of Geophysics, Faculty of Mathematics and Physics, Charles University, V Holešovičkách 2, Prague 8, 180 00, Czech Republic. (gallovic@karel.troja.mff.cuni.cz)